

**The location of the dense and ionized gas in the NGC 2023 PDR**F. Wyrowski <sup>1</sup>, C.M. Walmsley <sup>2</sup>, W.M. Goss <sup>3</sup> and A.G.G.M. Tielens <sup>4</sup>**ABSTRACT**

The VLA and the BIMA array were used to obtain high resolution (10–20'') observations of C<sup>+</sup>, traced by the C91 $\alpha$  recombination line at 8.6 GHz, and the dense molecular gas, traced by HCN and HCO<sup>+</sup>(1–0), of the photon dominated region (PDR) associated with the reflection nebula NGC 2023. Using the VLA, continuum emission is detected at 8.6 GHz from a faint HII region associated with HD 37903. The C91 $\alpha$  emission originates from a 0.4 pc long filament, extending from the east to the south of the exciting star HD 37903. Within the filament three C91 $\alpha$  clumps can be distinguished, each associated with filamentary vibrationally excited H<sub>2</sub> emission in the direction toward HD 37903. The HCO<sup>+</sup> emission has a clumpy appearance superimposed on a more extended component. C91 $\alpha$  is, in general, closer to the exciting star than HCO<sup>+</sup> emission as expected from PDR models. The morphologies of HCO<sup>+</sup> and HCN are quite similar. Based on the C91 $\alpha$  linewidth towards one of the clumps a limit of 170 K on the kinetic temperature in the ionized carbon layer can be derived. This value is consistent with PDR models with H<sub>2</sub> densities of about 10<sup>5</sup> cm<sup>-3</sup>. However, this result suggests surprisingly low limits on the turbulence in the PDR. We detected a compact 3 mm continuum source in the PDR, which appears to be a cold “core” of density 10<sup>7</sup> cm<sup>-3</sup>, 0.03 parsec diameter, and 6 M<sub>⊙</sub>. We conclude that it may have formed within the PDR.

In an appendix, observations of the C91 $\alpha$  recombination line toward five additional PDRs using the Effelsberg 100m telescope are described.

*Subject headings:* ISM: individual(NGC 2023) ISM: structure — radio lines: ISM — techniques: interferometric

---

<sup>1</sup>Department of Astronomy, University of Maryland, College Park, MD 20742-2421

<sup>2</sup>Osservatorio Astrofisico di Arcetri, Largo E. Fermi 5, I-50125 Firenze, Italy

<sup>3</sup>NRAO, Very Large Array, Very Long Baseline Array, P.O. Box 0, Socorro, NM 87801

<sup>4</sup>Kapteyn Astronomical Institute, Groningen

## 1. Introduction

Reflection nebulae are gas and dust clouds in the vicinity of hot young stars. On their surfaces, photon dominated regions (PDRs) exist due to the interaction of the newborn stars with their parental molecular environment leading to intense emission of fine structure lines of carbon and oxygen and of  $\text{H}_2$  ro-vibrational transitions ( $\text{H}_2^*$ ). A considerable fraction of the mass of the ISM is included in PDRs. They are also responsible for most of the FIR radiation in the Galaxy. Thus, our understanding of PDRs is a key astrophysical problem. Within a PDR, ionized carbon plays an important role in the molecular chemistry in the hot HI zone and H/ $\text{H}_2$  transition layer (Sternberg and Dalgarno 1995). Ionized carbon has mainly been traced to date using the carbon  $^2\text{P}_{3/2}$ - $^2\text{P}_{1/2}$  fine structure line at  $158 \mu\text{m}$ . However, observations of this transition are limited presently to resolutions of about 1 arc minute, corresponding to 0.15 parsec at the distance of the Orion nebula. There is, however, another way to approach the problem of determining the spatial distribution of ionized carbon. Radio observations of the carbon recombination lines can be used to analyze ionized carbon in PDRs (Natta et al. 1994). In this case the higher density regions of the PDR are selectively observed since the radio line intensity is proportional to the carbon emission measure.

This procedure has already been successfully carried out towards the PDR of the Orion Bar (Wyrowski et al. 1997a), leading to a view of the CII region with the highest spatial resolution to date (0.04 pc). A layer of carbon line emission bracketed between ionized and molecular media was detected. In contrast to predictions of current PDR models, the layer of ionized carbon is essentially coincident with  $\text{H}_2^*$  emission. Simple theory predicts that the radio recombination line should peak farther from the ionization front than molecular hydrogen. Thus, a possible discrepancy between observation and theory may exist. Hence, in order to obtain a more general knowledge of the properties of ionized carbon (CII) regions, investigations of further PDRs with different physical conditions are needed.

Here observations of the PDR in the reflection nebula NGC 2023 are presented, located at a distance of  $\approx 475$  pc in the Orion L 1630 molecular cloud and illuminated by the B1.5 V star HD 37903. This star is much less luminous than the exciting stars of the Orion nebula and the physical conditions are expected to be different. NGC 2023 has been the target of many observational studies including [CII]  $158 \mu\text{m}$  (Howe et al. 1991; Jaffe et al. 1994),  $\text{H}_2^*$  (Gatley et al. 1987; Field et al. 1994, 1998; McCartney et al. 1999; Martini et al. 1999), and CN and HCN (Fuente et al. 1995). In a recent study, the C91 $\alpha$  radio recombination line using the Effelsberg 100-m telescope towards this source was observed (Wyrowski et al. 1997b) suggesting densities of  $\sim 10^5 \text{ cm}^{-3}$ . Wyrowski et al. discuss several geometrical dependent models which help to constrain the physical parameters of the CII region by comparison with the other PDR tracers. Face- and edge-on models of the PDR were analyzed as well as clumpy models. A clear conclusion from this study was that improved angular resolution in the C91 $\alpha$  line was needed; thus the VLA was used to obtain improved resolution and further test the models.

In order to interpret the carbon line data, it is also useful to obtain molecular line observations

with similarly high angular resolution. We therefore decided to study the stratification between different PDR layers ( $\text{H}_2^*$ ,  $\text{CII}$ , molecules) with the aid of high angular resolution data for the molecular phase of this edge-on PDR. For this purpose, the high density tracers  $\text{HCO}^+$  and  $\text{HCN}$  were observed, expected to be abundant in layers where the influence of the ultraviolet radiation field is still appreciable. Here we report BIMA observations of these molecules with an angular resolution of 10 arc seconds, matching the VLA observations of the carbon line.

## 2. Observations

### 2.1. Carbon recombination line measurements with the VLA

NGC 2023 was observed with the VLA in the D array on Dec 8, 11 and 12, 1997. Table 1 summarizes the basic observing parameters. The phase center of the image was chosen to lie 1 arc minute south of HD 37903 ( $\alpha(2000) = 05^{\text{h}}41^{\text{m}}38^{\text{s}}.39$ ,  $\delta(2000) = -02^{\circ}15'32''.5$ ) 3C84 was observed for 13 minutes each day and was used for bandpass calibration. Phase calibrations were made on QSO 0607–085 every 25 minutes. The flux density scale was established by observations of 3C147, assuming a flux density of 4.74 Jy for this source.

At the  $\text{C91}\alpha$  observing frequency of 8.589104 GHz (Rohlfs and Wilson 1996) the correlator was used with a bandwidth of 1.5625 MHz. Hanning smoothing was applied during the data acquisition and the final spectral resolution is 6.1 kHz ( $0.2 \text{ km s}^{-1}$ ) with a total of 255 channels.

The data were processed using the AIPS package. The resultant synthesized beam is  $11.3'' \times 9.3''$  (PA= $-3^\circ$ ) with natural weighting and the final rms noise was 1 mJy/beam (0.16 K) in a channel image, consistent with the theoretical noise level. To increase the temperature sensitivity, also lower resolution images were obtained from tapered UV data which have synthesized beams of  $19.6'' \times 18.1''$  (PA= $1^\circ$ ) resulting in an rms noise of 1.2 mJy/beam (0.06 K). A 3.5 cm continuum image was produced by summing over the line free channels and the resulting rms is 0.1 mJy/beam.

Due to missing short spacings the largest angular scale imaged with the VLA is three arc minutes. From comparison of the integrated observed flux density with the single dish 100m results of Wyrowski et al. (1997b) we estimate that the VLA observations detect 55% of the peak  $\text{C91}\alpha$  flux density and 35% of the velocity integrated flux density (Fig. 1). To recover the missing flux density of the VLA observations, an additional image of the integrated  $\text{C91}\alpha$  intensity was constructed using the AIPS maximum entropy deconvolution task VTESS and the total flux density was forced to be consistent with the 100m telescope data (an average over all positions observed by Wyrowski et al. (1997b)).

## 2.2. C65 $\alpha$ observation with the 100-m telescope

Additionally, an observation of the C65 $\alpha$  carbon recombination line was obtained with the Effelsberg 100m telescope toward one position ((0", -80") relative to HD 37903) of NGC 2023 on Dec 2, 1997. Calibration was made relative to NGC 7027, assuming a flux density of 5.5 Jy for this source at the observing frequency of 23.4159609 GHz. The angular resolution of the telescope at this frequency is 40".

## 2.3. HCO<sup>+</sup> and HCN observations with BIMA

The BIMA array (Welch et al. 1996) was used in its C and D configuration for four tracks on NGC 2023 between May and August 1999 obtaining baselines from 6 to 85 m. A 3 pointing mosaic was observed, separated by 67", covering the range of the C91 $\alpha$  emission. Every 20 min the phase calibrator QSO 0609–157 was observed. Jupiter was used to establish the flux density calibration leading to flux densities between 5 and 7.5 Jy for the potentially variable quasar QSO 0609–157 on different days. HCO<sup>+</sup> and HCN were observed in the lower sideband with a spectral resolution of 0.1 MHz (0.3 km s<sup>-1</sup>) and 256 spectral channels each. All calibration and image deconvolution was carried out using the MIRIAD package: averaged line emission images were constructed using a robustness parameter of 0 leading to a beam size of 11.2"  $\times$  8.1" (PA=-7°). To increase the temperature sensitivity, line cubes were also made with natural weighting leading to a beam size of 15.8"  $\times$  10.7" (PA=-6°). All the images were deconvolved using a maximum entropy algorithm (MIRIAD task mosmem). The rms noise in the channel images is  $\sim$  0.2 Jy/beam, close to the theoretical noise level. Since the single dish HCN observations of Fuente et al. (1995) cover parts of our image, it was possible to estimate for a few positions the missing flux density of the interferometer data and found that the BIMA HCN image contains typically 70% of the single dish flux density.

A 3 mm continuum image was produced as well by summing over the line free channels and both sidebands. The beam size of the image is 15.5"  $\times$  10.5" (PA=-6°) and the rms is 2.5 mJy/beam.

## 3. Results

### 3.1. The 8 GHz continuum source associated with HD 37903

From the VLA continuum image<sup>5</sup>, a weak, extended ( $\sim$  40" or 0.1 pc) source with an integrated flux density of  $8.5 \pm 1$  mJy is detected (Fig. 2). The emission peaks (-10", -12") offset from HD 37903, corresponding to a projected distance of 0.035 pc from the exciting star. There is no

evidence for continuum emission associated with the PDR.

We assume that the observed continuum emission is due to optically thin free-free radiation from gas ionized by HD 37903. This is consistent with the low observed peak brightness temperature of 0.12 K. The evidence suggests that the stellar Lyman continuum flux is incident upon a nearby density enhancement. We find for an electron temperature of 10000 K that the observed flux density is due to a region with an electron density of  $200 \text{ cm}^{-3}$  or an emission measure of  $3000 \text{ cm}^{-6} \text{ pc}$ . The Lyman continuum flux to maintain the ionization is  $\log(N_C) = 44.26 \text{ s}^{-1}$ , corresponding to ionization by a B2.5 V star (Panagia 1973). This value is in contrast to the observed optical spectral classification of B1.5 V (Racine 1968) which suggests either a density bounded HII region or that a considerable fraction of Lyman continuum photons are absorbed in lower density more extended material not detected by the interferometer, thus lowering the spectral type estimate.

There are, however, no molecular line features on our BIMA images associated with the HII region though there does appear to be some associated molecular hydrogen just south of HD 37903 (see Fig. 3). In addition, a streamer of C91 $\alpha$  emission reaches from the CII filament up to the HII region. We presume therefore that the “nearby density enhancement” contains rather little neutral gas (corresponding to a column density of at most  $10^{21} \text{ cm}^{-2}$ ) but that it should be observable in H $\alpha$  and other tracers of ionized gas.

### 3.2. Carbon recombination line image with the VLA

Images of the C91 $\alpha$  emission averaged over the line are presented in Fig. 2 with angular resolutions of 10 and 20". The carbon recombination line emission originates from a filament of roughly 3 arc minutes in length (0.4 pc) which extends from the east to the south of HD 37903. The projected distance from the exciting star varies between 0.13 and 0.17 parsec. Three emission maxima can be distinguished, positions 1, 2, and 3 (Fig. 2). On Fig. 2, also spectra averaged over 20" regions are shown centered on those maxima. Table 2 lists the derived line parameters toward these positions.

Based on the VLA data, the emission is resolved with 10 arc second resolution. The width (perpendicular to the filament) of the C91 $\alpha$  emission is in the range 10–40" (0.02–0.08 pc) along the filament. There is no evidence for clumping on angular scales smaller than 10", as had been earlier found for molecular hydrogen emission (Field et al. 1998). The 20" resolution image shows the emission with a higher dynamical range. In the remainder of the paper only images with this angular resolution are considered.

As discussed in Sect. 2.1, there is evidence for extended emission not detected by the VLA. Figure 1 shows the result of a comparison of the 100-m profile of C91 $\alpha$  with our VLA results, both

---

<sup>5</sup>FITS images of the maps shown in this paper may be obtained at URL <http://imaginglib.ncsa.uiuc.edu>

integrated over the whole emission area. Some of the blue wing emission observed with the 100m is absent in the VLA data. Figures 3 and 4 show integrated C91 $\alpha$  images with the total flux density fixed to the 100m value during the deconvolution. The main difference with the image in Fig. 2 is an additional halo of C91 $\alpha$  around the clumps. This halo is brighter toward the exciting star and the emission decreases sharply away from the star.

Fig. 5 shows a position–velocity plot of the C91 $\alpha$  emission along the filament averaged over 40'' perpendicular to the filament. Across clump 1 (Fig. 2), a velocity gradient of 7 km s<sup>−1</sup> pc<sup>−1</sup> is clearly observed, possibly reflecting rotation of the clump. The remainder of the filament is quiescent with linewidths of  $\sim 0.8$  km s<sup>−1</sup> (see clump 2 in Table 2). An overall view of the velocity structure is given in Fig. 6, where a comparison of C91 $\alpha$  with the corresponding molecular line channel images is shown.

The line observed in the direction of clump 2 is quite narrow ( $\sim 0.8$  km s<sup>−1</sup>). The observed linewidth can be used to impose a stringent upper limit on the clump kinetic temperature  $T_{\text{kin}}$ . For purely thermal broadening, the linewidth  $\Delta v_{th}$  (in km s<sup>−1</sup>) will be given by:

$$\Delta v_{th}^2 = 0.0458 T_{\text{kin}}/M(\text{AMU}), \quad (1)$$

where  $M = 12$  is the mass of the emitting species in AMU. From this, we derive an upper limit of 170 K. The line width toward clump 1 is larger, however, as discussed in the previous paragraph, it is dominated by the velocity gradient seen in Fig. 6 and *not* by an increase in the kinetic temperature. Thus the limit which we derive for clump 2 may be valid along the whole filament.

From the [CII] 158  $\mu\text{m}$  fine structure line intensity, a lower limit on the temperature of 138 K can be derived (Steiman-Cameron et al. 1997). Using the ratio of C91 $\alpha$  and [O I] 63  $\mu\text{m}$  emission, Wyrowski et al. (1997b) derived a temperature range of 100–300 K. Another lower limit on the temperature is the line intensity of the CO(7–6) line measured by Jaffe et al. (1990), which indicates a temperature of  $> 85$  K. In PDR models, the higher CO lines originate from about the same depth in the PDR as the carbon recombination line (i. e. the surface of the C<sup>+</sup>/C/CO transition zone). These estimates are close to the upper limit inferred from the line width above. This agreement could suggest that the major line broadening agent is thermal and that the turbulent broadening is less than  $\sim 0.4$  km s<sup>−1</sup>. This value is in contrast to the situation in neighboring molecular layers (see Sect. 3.4) deeper in the PDR where the temperature is likely to be lower; without turbulent broadening the widths of the molecular lines would be considerably smaller than the C91 $\alpha$  line widths but are observed to be similar to the C91 $\alpha$  line width. We conclude that the Alfvén waves or other turbulent agents which give rise to non-thermal broadening in the molecular gas do not penetrate very much into the higher ionization degree layer associated with the C91 $\alpha$  emission.

Similar conditions may prevail in the reflection nebula NGC 7023 where the 100-m observation of C91 $\alpha$  (see Appendix) indicate a rather similar limit on the temperature. Thus, we conclude that the temperature in the ionized carbon layers of PDRs excited by early B-stars with incident radiation fields similar to that estimated in NGC 2023 (smaller than 10<sup>4</sup> times the average interstellar FUV field) is likely to be of order 200 K or lower.

The observed spectral range covers the frequency of the sulfur (as well as Si and Mg) radio recombination lines. This line has been detected in several PDRs (Silverglate 1984) but not in the Orion Bar or NGC 2023. No S91 $\alpha$  lines were detected in the VLA data by averaging over carbon line emission regions, in which the C91 $\alpha$  line was detected with a signal-to-noise ratio of 10. Therefore the  $2\sigma$  upper limit for the ratio of sulfur to carbon line intensities is 0.2, consistent with solar abundances (Grevesse et al. 1996, C/H=3.6 $\times 10^{-4}$  and S/H=2.1 $\times 10^{-5}$ ) and also with depletion of C by the factor observed in nearby diffuse clouds (Sofia et al. 1997, C/H=1.4 $\times 10^{-4}$ ) and solar abundance for S. However, this limit rules out strong deviations from the C/S cosmic abundance ratio due to depletion of carbon on grains which was earlier found for S88B by Silverglate (1984) and Garay et al. (1998).

### 3.3. C65 $\alpha$ line emission with the 100-m

Figure 7 shows the C65 $\alpha$  carbon recombination line spectrum observed toward NGC 2023. This observation is the highest frequency at which the carbon line in NGC 2023 has been detected to date. Based on this detection it is possible to constrain the departure coefficients for principle quantum numbers  $n$  between 65 and 91; thus, in principle, the density and temperature in the PDR can be constrained. The C91 $\alpha$  VLA total flux corrected image was convolved to a 40'' beam and a ratio of the integrated intensities  $I_{91}/I_{65}$  of C91 $\alpha$  and C65 $\alpha$  of  $2.4 \pm 0.7$  was estimated. The ratio of departure coefficients  $b_{91}/b_{65}$  (see Eq. 7.3 of Wyrowski (1997) for the case with no continuum) is:

$$b_{91}/b_{65} = \exp(18.28/T) (I_{91}\nu_{91})/(I_{65}\nu_{65}). \quad (2)$$

We conclude that for a temperature  $T$  of 150 K based on the above discussion, the measured intensity ratio implies  $b_{91}/b_{65} = 1 \pm 0.3$ . This value compares with a value of 1.5–2 for  $b_{91}/b_{65}$  expected on the basis of conventional hydrogenic recombination theory (Salem and Brocklehurst 1979) with an electron density in the range 3–30 cm $^{-3}$  and temperature  $\sim 150$  K. Hence, we cannot explain this result by conventional hydrogenic recombination theory. As was the case for the Orion Bar (Wyrowski et al. 1997a), dielectronic recombination (Walmsley and Watson 1982) seems most likely.

### 3.4. Molecular line emission images

Channel images of the HCO $^+$  and HCN emission are shown in Fig. 6, sampled with the same velocity grid as the C91 $\alpha$  emission. The brighter HCO $^+$  emission is shown in greyscale with a complex, clumpy structure. All the bright HCO $^+$  features are also observed in HCN. Differences between the two molecular transitions are discussed below.

Figure 8 shows averaged spectra toward the two positions with strongest emission. The hyperfine satellites of HCN ( $F = 2 - 1, 1 - 1, 0 - 1$ ) are clearly detected with integrated intensity ratios of

(1:0.44:0.26) at offset (52'', -43'') and (1:0.52:0.33) at offset (34'', -96'') from HD 37903, respectively. These ratios are clearly different from the values expected in the optically thin LTE limit (1:0.6:0.2) and moreover the  $F = 1 - 1/2 - 1$  ratio is  $< 0.6$  and thus incompatible with the ratios expected in LTE at any optical depth. Such anomalies in the HCN  $J = 1 - 0$  hyperfine satellite line ratios are well known (Guilloteau et al. 1981; Walmsley et al. 1982; Gonzales-Alfonso and Cernicharo 1993) and can be explained as being due to the combination of moderate opacity and line overlap. Indeed, the calculations of (Guilloteau et al. 1981, Fig. 2) are able to reproduce our results toward the position (52'', -43''), where we detected the hyperfine satellites with brightness temperatures of (5.3 K, 2.2 K, 1.3 K), corresponding to  $N(\text{HCN}) \approx 5 \times 10^{12} \text{ cm}^{-2}$  in their model with  $T_{\text{kin}}=30 \text{ K}$  and  $n(\text{H}_2) = 10^5 \text{ cm}^{-3}$ .

Moderate opacity is also suggested by the fact that the line profiles of HCN and  $\text{HCO}^+$  agree. The northern clump (upper panel) shows a line width of  $0.8 \text{ km s}^{-1}$ , whereas the southern clump (lower panel) splits up into two velocity components separated by  $1.6 \text{ km s}^{-1}$ . This latter result suggests the presence of at least two clumps of higher density material with differing velocities immersed in the PDR.

For the HCN and  $\text{HCO}^+(1-0)$  lines, the upper energies and critical densities are quite similar. Hence changes in the relative intensities should reflect changes in the relative abundances of the two molecules. Fig. 9 shows the ratio of HCN and  $\text{HCO}^+$  emission superimposed on the integrated  $\text{HCO}^+$  image. Toward the emission peaks, the HCN/ $\text{HCO}^+$  ratio is reduced by a factor of two compared to the surroundings. In the southern clump, there is evidence for a gradient of the HCN/ $\text{HCO}^+$  ratio, decreasing from 0.8 at the northern edge to 0.3 to the south. Fuente et al. (1993) have constructed chemical models which include HCN and  $\text{HCO}^+$  using densities and temperatures similar to NGC 2023. In their models the  $\text{HCO}^+$  abundance decreases significantly for  $A_v < 6$  due to the increasing electronic abundance. This effect might explain the increased HCN/ $\text{HCO}^+$  ratio toward the edges of the PDR.

### 3.5. 3 mm continuum results

Within the observed mosaic, one resolved millimeter continuum source is detected at (-19'', -106'') offset from HD 37903 (Fig. 4). The deconvolved size of the emission is 12'' (0.028 pc) with an integrated flux density of  $36 \pm 7 \text{ mJy}$ . Based on the noise in our 8 GHz continuum image we can estimate an upper limit on free-free emission at 3 mm of 9 mJy, assuming optically thick emission from 8 to 85 GHz. A more realistic turnover from optically thick to thin emission at intermediate observing frequencies would lead to corresponding lower limits on free-free emission at 3 mm. Thus, thermal dust emission must be the primary mechanism for the 3 mm continuum. Using the equation for the corresponding mass given by Mezger et al. (1990) with the dust cross section estimates by Rengarajan (1984) for dust with ice mantles, a dust opacity index of 2, and a temperature of 20 K, we find a clump mass of  $6 M_{\odot}$ . The central column density of  $\text{H}_2$  is then  $10^{24} \text{ cm}^{-2}$  corresponding to a visual extinction of  $\sim 1000 \text{ mag}$  and an average molecular hydrogen



density of  $10^7 \text{ cm}^{-3}$ .

Dust emission toward this position was first detected by Launhardt et al. (1996) with the SEST telescope at 1.3 mm; however with the lower angular resolution of  $23''$  and a lower S/N no well-defined compact clump, as detected at 3 mm, was found. Fig. 4 shows a comparison of the 3 mm continuum emission with a  $850 \mu\text{m}$  SCUBA image (G. Sandell 1999, priv. comm.) and the C91 $\alpha$  and HCN line emission. The 3 mm source is coincident with compact  $850 \mu\text{m}$  emission detected by SCUBA, confirming the interpretation that the source is caused by dust emission. Indeed it seems likely to be a cold “prestellar core”, as the SCUBA detection is consistent with a temperature of 20 K. No IRAS source is at this position, however the IRAS images of this region are very confused. There seems to be a source associated with the core in a recent ISOCAM image of NGC 2023 (Nordh et al., in preparation), but no flux density estimates are available yet. The core is also coincident within the errors with star 3 of the DePoy et al. (1990) NIR observations, who find this star to be the reddest object in the NGC 2023 star cluster with about 30 mag of visual extinction, assuming that the star is on the main sequence. This extinction is still far smaller than the one derived for the millimeter core. Hence, the star seems to lie in the foreground of the dense millimeter clump, but is still considerably embedded in the outer portion of the clump to account for the reddening. Alternatively, the NIR emission might be due to scattered light from a more embedded source, since the emission seems to be resolved in the NIR images of Field et al. (1998) and McCartney et al. (1999).

The 3 mm core has no prominent counterpart in HCN or HCO<sup>+</sup> emission. However, there is weak HCO<sup>+</sup> emission towards the 3 mm continuum source with a linewidth of  $0.8 \text{ km s}^{-1}$ . Combining this linewidth with the size estimate leads to a “virial” mass for the continuum source of roughly  $2 M_{\odot}$ . In addition,  $30''$  to the NE of the 3 mm source, a prominent feature in the HCN, HCO<sup>+</sup> and the C91 $\alpha$  images is observed with a velocity of  $10.85 \text{ km s}^{-1}$  (Fig. 6). The emission seems to originate from a small clump which appears to be on the surface of the 3 mm core. We will discuss this in more detail in Sect. 5.

## 4. Comparison of different PDR tracers

### 4.1. Vibrationally excited molecular hydrogen emission

By using observations of vibrationally excited molecular hydrogen in the NIR, angular resolutions of  $\sim 1''$  can be achieved in the photodissociated gas (Field et al. 1998; Rouan et al. 1997). These lines originate from a thin cloud layer and are excited by the stellar UV radiation. At these surfaces carbon is ionized and can emit recombination lines. It is therefore of interest to compare H<sub>2</sub><sup>\*</sup> and C91 $\alpha$ .

Figure 3 shows an overlay of C91 $\alpha$  emission with vibrationally excited H<sub>2</sub> (Field et al. 1998). The coordinate system of the H<sub>2</sub><sup>\*</sup> image was established using the position of the star HD 37903

and the scale and orientation given by (Field et al. 1998). In addition, the positions of all the stars measured in previous NIR studies (Sellgren 1983; DePoy et al. 1990) are plotted on top of the  $H_2^*$  image. The astrometry of the  $H_2^*$  image seems to agree more with the Sellgren (1983) positions and we consider the offsets of up to  $8''$  of the DePoy et al. (1990) positions to be due to a small stretch and rotation of their image. The C91 $\alpha$  clumps are systematically offset from the  $H_2^*$  filamentary emission, displaced away from the exciting star HD 37903. This displacement suggests that the  $H_2^*$  emission arises from limb brightening at the edge of the C91 $\alpha$  clumps. However, some of the  $H_2^*$  streamers are *not* associated with C91 $\alpha$  emission. The offsets between the peak emission of C91 $\alpha$  and  $H_2^*$  for the clumps referred to in Fig. 2 are 10, 4, and  $7''$ , respectively. This effect is shown in detail in the cross-cuts shown in Fig. 10. Stationary PDR models suggest a displacement between these components by  $N_H \approx 4 \times 10^{21} \text{ cm}^{-2}$  (Hollenbach et al. 1997,  $A_v \approx 2$ ). Hence, assuming edge-on geometry, gas with an atomic hydrogen density of  $6\text{--}14 \times 10^4 \text{ cm}^{-3}$ , could account for the observed offset (see the discussion in Sect. 5).

## 4.2. HCO<sup>+</sup> emission

The dense molecular cloud adjacent to NGC 2023 is revealed by the high  $H_2$  density tracer HCO<sup>+</sup> ( $n_{\text{cr}} \sim 10^{4.5} \text{ cm}^{-3}$ ). Figure 3 compares the carbon recombination line results with the BIMA HCO<sup>+</sup> velocity averaged image. The C91 $\alpha$  filament follows precisely the edge of the extended HCO<sup>+</sup> emission. However, the two southern peaks of the C91 $\alpha$  emission seem to be bracketed by the HCO<sup>+</sup> emission. This effect can be seen most clearly in the lower panel of Fig. 10, where the cross-cut through the southernmost C91 $\alpha$  peak reveals HCO<sup>+</sup> in front of and behind C91 $\alpha$ , while HCO<sup>+</sup> is weak at the C91 $\alpha$  peak position.

The HCO<sup>+</sup> emission can also be compared with the location of vibrationally excited  $H_2$ : low level HCO<sup>+</sup> emission seems to trace the same material as the  $H_2^*$  emission in front of the C91 $\alpha$  emission peaks indicating that some HCO<sup>+</sup> can survive even in the outermost PDR layers. This effect was also seen by Fuente et al. (1996) in NGC 7023. HCO<sup>+</sup> can be formed in the radical zone of a PDR through reactions of O with  $\text{CH}_2^+$  and  $\text{CH}_3^+$  or reactions of  $\text{C}^+$  with OH (Sternberg and Dalgarno 1995).

## 5. PDR model results

To interpret the observed projected offsets between the carbon recombination line and vibrationally excited  $H_2$  emission (Sect. 4.1), the intensities of these PDR tracers in a PDR model proposed by Tielens and Hollenbach (1985) are calculated with  $n_H = 10^5 \text{ cm}^{-3}$ ,  $G_0 = 10^4$ , and  $X[\text{C}] = 1.4 \times 10^{-4}$ , where  $G_0$  is the incident FUV field in units of the average flux of the interstellar medium. For an estimate of  $G_0$  in NGC 2023 the results of Steiman-Cameron et al. (1997) were used. The physical and chemical conditions of the model shown in Fig. 11 can account for

the observed offsets; on the other hand, we cannot rule out deviations from an edge-on geometry. Therefore the actual offsets between C91 $\alpha$  and H<sub>2</sub>\* might be larger with a resultant decrease in the density. As can be seen in Fig. 11, the upper limits on the temperature in the CII region from the measured line widths are consistent with the temperature predictions of the PDR model. The bulk of the C91 $\alpha$  emission originates from a depth in the PDR, where the temperature is 100–200 K. The calculated C91 $\alpha$  intensity is within a factor two equal to the observed values (Table 2).

In a clump of sufficiently high density, the positional offset between the molecular line and carbon line emission should become quite small. The models suggest that the difference in the depths in the PDR should be roughly  $A_v \sim 3$ . This corresponds to  $\sim 0.45/n_6$  arc seconds at the distance of NGC 2023, where  $n_6$  is the H<sub>2</sub> density in units of  $10^6 \text{ cm}^{-3}$ . Thus the offsets will be difficult to measure at densities much above  $10^5 \text{ cm}^{-3}$ . We do in fact observe a clump where there is rough coincidence between the peaks of C91 $\alpha$ , HCN, and HCO<sup>+</sup>. This object is associated with the 3 mm continuum source, discussed in Sect. 3.5. We conclude that this density must be significantly higher than  $10^5 \text{ cm}^{-3}$ .

## 6. Discussion and Conclusions

The current results indicate that the carbon recombination line emission, tracing the ionized carbon content of the NGC 2023 PDR, originates from the edge of the dense molecular cloud as observed in the high density tracers HCN and HCO<sup>+</sup>. C91 $\alpha$  emission bracketed between the molecular tracers and the exciting star is observed, as expected based on models of PDRs. The C91 $\alpha$  appears also to be offset relative to vibrationally excited H<sub>2</sub>, consistent with an atomic hydrogen density of  $10^5 \text{ cm}^{-3}$ .

The linewidth estimates for C91 $\alpha$  towards clump 2 place an upper limit of 170 K on the kinetic temperature in the ionized carbon layer. This value is in fact not much larger than *lower limits* on the temperature derived independently by Steiman-Cameron et al. (1997) and Wyrowski et al. (1997b). We conclude that line broadening due to turbulent motions is of minor importance in the PDR and that the energy density in turbulence is small. This finding may have consequences for the possibility of stars forming within the PDR.

An important result of our BIMA observations is the detection of the compact 3 mm continuum source. There is no IRAS source associated with it, but it is detected as a compact dust core at 850  $\mu\text{m}$  (G. Sandell 1999, priv. comm.). Furthermore, there is little sign of its presence in molecular lines. These facts argue that the core is cold and therefore starless. Molecules seem to be frozen-out onto grain surfaces, since no prominent molecular line emission is detected in the direction of the core.

The findings suggest that the dust core detected by BIMA is in the process of collapsing to form a protostar. Observations in other tracers can be important in order to test whether the absence of associated HCN and HCO<sup>+</sup> is a general phenomenon or is confined to those two species. The

detection of molecular lines associated with the object would considerably help in understanding its evolutionary state. From the density estimate of  $10^7 \text{ cm}^{-3}$  inferred from the continuum results, we derive a free-fall time of  $10^4$  years. This time is an order of magnitude less than the timescale expected for evolution of the PDR taking a size scale of 0.04 parsec and a velocity of  $0.5 \text{ km s}^{-1}$ . A possible scenario is that the dust core formed within the PDR with the formation triggered by the higher pressures resulting from the PDR heating. On the other hand, there is no evidence for interaction of the FUV radiation field with the BIMA/SCUBA core in the form of  $\text{C91}\alpha$  emission. However, the radiation field does seem to be interacting with the clump to the NE observed in  $\text{HCO}^+$  and  $\text{HCN}$  and it seems unlikely that the two clumps are adjacent only due to a chance projection.

We would like to thank Jean-Louis Lemaire for providing the  $\text{H}_2^*$  image of NGC 2023 and Goeran Sandell for providing the SCUBA image of NGC 2023 prior to publication. FW is supported by the National Science Foundation under Grant No. 96-13716. The research of CMW is partially supported by the ASI grant ARS-98-116 and by the MURST project “Dust and Molecules in Astrophysical Environments”. The National Radio Astronomy Observatory is a facility of the National Science Foundation operated under cooperative agreement by Associated Universities, Inc.

### A. $\text{C91}\alpha$ Effelsberg 100m observations

We have searched for emission in the  $\text{C91}\alpha$  radio recombination line towards several other star forming regions harboring PDRs using the Effelsberg 100m telescope. A more detailed description of the observations is given in Wyrowski (1997). The observations were carried out in July and August 1996. Table 3 gives a list of the observed sources and Fig. 12 shows the observed lines. The frequency of the observed  $\text{C91}\alpha$  lines is 8589.104 MHz with a beamsize of  $82''$ . Pointing was checked through observation on NGC 7027, W3(OH), and 3C161. Observations of NGC 7027 were used to establish the brightness temperature scale assuming a continuum flux density of 6.25 Jy and a telescope sensitivity of 2.7 K/Jy. DR 21 was observed in position switching mode and all other sources in frequency switching mode. The spectrometer was an autocorrelator yielding a spectral resolution of  $0.2 \text{ km s}^{-1}$  in case of NGC 7023 and  $0.4 \text{ km s}^{-1}$  for the other sources. The average integration time on a source was 7 hours. In Table 4 the results of Gaussian fits to the observed spectra are listed. In case of the three non-detections the  $1\sigma$  level of the noise in the observed spectra is given. An important result to note is the extremely narrow  $\text{C91}\alpha$  line in NGC 7023. The linewidth is clearly smaller than the widths of  $\text{H}_2^*$  and  $\text{CII } 158 \mu\text{m}$  (Lemaire et al. 1999; Gerin et al. 1998), indicating that the latter emissions originate from a hotter surface layer of the PDR. Using Eq. 1 we estimate an upper limit of the temperature in the  $\text{CII}$  zone of 190 K. This value is quite similar to the limit we derived for NGC 2023.

## REFERENCES

- DePoy D.L., Lada E.A., Gatley I., Probst R. 1990, ApJ 356, L55
- Field D., et al. 1994, A&A 286, 909
- Field D., et al. 1998, A&A 333, 280
- Fuente A., Martin-Pintado J., Cernicharo J., Bachiller R. 1993, A&A 276, 473
- Fuente A., Martin-Pintado J., Gaume R. 1995, ApJ 442, L33
- Fuente A., Martin-Pintado J., Neri R., Rogers C., Moriarty-Schieven G. 1996, A&A 310, 286
- Garay G., Gomez Y., Lizano S., Brown R.L. 1998, ApJ 501, 699
- Gatley I. et al. 1987, ApJ 318, L73
- Gerin M., Phillips T.G., Keene J., Betz A.L., Boreiko R.T. 1998, ApJ 500, 329
- Gonzales-Alfonso E., Cernicharo J. 1993, A&A 279, 506
- Grevesse N., Noels A., Sauval A. J. 1996, ASP Conf. Ser. 99: Cosmic Abundances, 117
- Guilloteau S., Baudry A. 1981, A&A 97, 213
- Hollenbach D.J., Tielens A.G.G.M. 1997, ARAA 35, 179
- Howe J.E., Jaffe D.T., Genzel R., Stacey G.J. 1991, ApJ 373, 158
- Jaffe D.T., Genzel R., Harris A.I., Howe J.E., Stacey G.J., Stutzki J., 1990, ApJ 353, 193
- Jaffe D.T., et al. 1994, ApJ 436, 203
- Launhardt R., Mezger P.G., Haslam C.G.T., Kreysa E., Lemke R., Sievers A., Zylka R. 1996, A&A 312, 569
- Lemaire J.L., Field D., Maillard J.P., Pineau des Forets G., Falgarone E., Pijpers F.P., Gerin M., Rostas F. 1999, A&A 349, 253
- Martini P., Sellgren K., DePoy D.L. 1999, ApJ 526, 772
- McCartney M.S.K., Brand P.W.J.L., Burton M.G., Chrysostomou A. 1999, MNRAS 307, 315
- Mezger P.G., Wink J.E., Zylka R. 1990, A&A 228, 95
- Natta A., Walmsley C.M., Tielens A. 1994, ApJ 428, 209
- Panagia N. 1973, AJ 78, 929

- Racine R. 1968, AJ 73, 233
- Rengarajan T.N. 1984, A&A 140, 213
- Rohlfs K., Wilson T.L. 1996, “Tools of Radio Astronomy”, Springer
- Rouan D., Field D., Lemaire J.-L., Lai O., Pineau des Forets G., Falgarone E., Deltorn J.-M. 1997, MNRAS 284, 395
- Salem M., Brocklehurst M. 1979, ApJS 39, 633
- Sellgren K. 1983, AJ 88, 985
- Silverglate P.R. 1984, ApJ 278, 604
- Sofia U.J., Cardelli J.A., Guerin K.P., Meyer D.M. 1997, ApJ 482, L105
- Steiman-Cameron T.Y., Haas M.R., Tielens A.G.G.M, Burton M.G. 1997, ApJ 478, 261
- Sternberg A., Dalgarno A. 1995, ApJS 99, 565
- Tielens A. , Hollenbach D. 1985, ApJ 291, 722
- Walmsley C.M. , Churchwell E., Nash A., Fitzpatrick E. 1982, ApJ 260, 317
- Walmsley C.M., Watson W.D. 1982, ApJ 260, 317
- Welch W.J. et al. 1996, PASP 108, 93
- Wyrowski F., Walmsley C.M., Hofner P., Schilke P. 1997, ApJ 487, L171
- Wyrowski F., Walmsley C.M., Natta A., Tielens A. 1997b, A&A 324, 1135
- Wyrowski F. 1997, PhD. thesis, University of Cologne

Table 1: VLA Observing Parameters

|                                |  |
|--------------------------------|--|
| Rest Frequency (C91 $\alpha$ ) | 8.589104 GHz   |
| Total Bandwidth                | 1.5625 MHz   |
| Number of Channels             | 255  |
| Channel Separation             | 6.1 KHz (0.21 km s <sup>-1</sup> )                     |
| Synthesized Beam FWHM          | 11.3 x 9.3 arcsec, PA=-3°                              |
| Tapered Beam FWHM              | 19.6 x 18.1 arcsec PA=1°                               |
| Primary Beam FWHM              | 5.2 arcmin   |
| Phase Center                   | $\alpha_{2000} = 5:41:38.4$ $\delta_{2000} = -2:16:32$ |
| Time On Source                 | 9.7 hours  |

Table 2: Line parameters of the averaged spectra shown in Fig. 2.

| clump #       | offsets<br>(arcsec) | $T_L$<br>(K) | $v_{\text{LSR}}$<br>(km s <sup>-1</sup> ) | $\Delta v$<br>(km s <sup>-1</sup> ) |
|---------------|---------------------|--------------|---|-------------------------------------|
| NGC2023:CII 1 | (-7, -88)           | 0.36±0.05    | 10.31±0.05                                | 1.3±0.1                             |
| NGC2023:CII 2 | (25, -64)           | 0.49±0.06    | 9.97±0.03                                 | 0.8±0.1                             |
| NGC2023:CII 3 | (56, -7)            | 0.16±0.05    | 10.0±0.1                                  | 1.9±0.3                             |



Table 3: Sources observed in the C91 $\alpha$  carbon recombination line.

| Source       | $\alpha(2000)$<br>h m s | $\delta(2000)$<br>° ' " |
|--------------|-------------------------|-------------------------|
| IC 63        | 00 59 01.4              | 60 53 17.604            |
| RMC (IR6306) | 06 33 16.1              | 04 34 56.788            |
| S 106        | 20 27 26.6              | 37 22 47.872            |
| NGC 7023     | 21 01 37.2              | 68 09 46.587            |
| DR 21        | 20 39 01.0              | 42 19 29.855            |
| DR 21 (OH)   | 20 39 00.7              | 42 22 32.841            |

Table 4: C91 $\alpha$  line parameters. For non-detection the  $1\sigma$  noise level in the spectrum is given.

| Source       | Offsets<br>(arcsec) | $\int T_{\text{MB}} dv$<br>(K km s $^{-1}$ ) | $T_{\text{MB}}$<br>(K) | $v_{\text{LSR}}$<br>(km s $^{-1}$ ) | FWHM<br>(km s $^{-1}$ ) |
|--------------|---------------------|--|------------------------|-------------------------------------|-------------------------|
| IC 63        |                     |  | 0.01                   |                                     |                         |
| RMC (IR6309) |                     |  | 0.01                   |                                     |                         |
| S 106        | (0, 0)              | 0.69 $\pm$ 0.03                              | 0.07 $\pm$ 0.02        | -4.0 $\pm$ 0.2                      | 8.9 $\pm$ 0.5           |
| S 106        | (30, -30)           | 0.40 $\pm$ 0.04                              | 0.04 $\pm$ 0.02        | -3.5 $\pm$ 0.2                      | 9.8 $\pm$ 1.1           |
| NGC 7023     | (-20, 30)           | 0.11 $\pm$ 0.01                              | 0.12 $\pm$ 0.02        | 2.3 $\pm$ 0.05                      | 0.88 $\pm$ 0.08         |
| NGC 7023     | (0, 0)              | 0.05 $\pm$ 0.02                              | 0.07 $\pm$ 0.02        | 2.6 $\pm$ 0.12                      | 0.8 $\pm$ 0.2           |
| DR 21        |                     | 0.76 $\pm$ 0.08                              | 0.07 $\pm$ 0.02        | -5.1 $\pm$ 0.4                      | 10 $\pm$ 1              |
| DR 21 (OH)   |                     |  | 0.01                   |                                     |                         |

Fig. 1.— Integrated emission of Effelsberg 100m measurements of the C91 $\alpha$  carbon recombination line (80'' beam) compared with the integral over the VLA observation (grey histogram).

Fig. 2.— Radio continuum (greyscale) and C91 $\alpha$  carbon recombination line emission (contours) toward NGC 2023 observed with the VLA. Line emission is averaged from  $v_{\text{LSR}}$  9.6–11.1 km s<sup>-1</sup>. The left panel shows natural weighting images ( $\sim 10''$  beam) and the middle panel smoothed images ( $\sim 20''$  beam) using a uv-taper to emphasize emission on larger scales. Contours and greyscales start at  $3\sigma$  and advance in  $2\sigma$  steps. For the line emission the  $-3\sigma$  dashed contour is also shown. The noise in the continuum and C91 $\alpha$  images in both panels are, respectively, 0.085, 0.41, 0.13 and 0.45 mJy/beam. The right panels show spectra of the C91 $\alpha$  line averaged over  $20''$  regions centered on the clumps labeled in the middle panel. Parameters of the Gaussian fits (dotted lines) are given in Table 2.

Fig. 3.— Comparison of the locations of C91 $\alpha$  emission (thick contours, maximum entropy deconvolution, cf. Sect. 2.1) with those of vibrationally excited H<sub>2</sub> (Field et al. 1998, thin contours) and HCO<sup>+</sup> (greyscale). The C91 $\alpha$  emission is averaged from 9.6–11.1 km s<sup>-1</sup> and the contours are 3,5,7...  $\times 0.4$  mJy/beam ( $19.6'' \times 18.1''$  beam). The HCO<sup>+</sup> emission is averaged from 8.53–11.5 km s<sup>-1</sup> and the contours are 3,6,9...  $\times 0.1$  Jy/beam ( $11.2'' \times 8.1''$  beam). As a check of the astrometry of the NIR image, the positions of the NIR sources (Sellgren 1983; DePoy et al. 1990; see corresponding markers) are shown. For the H<sub>2</sub> and the HCO<sup>+</sup> data the boundaries of the observations are outlined.

Fig. 4.— Comparison of the locations of C91 $\alpha$  emission (same as in Fig.3) with those of 850  $\mu\text{m}$  dust emission (greyscale, G. Sandell 1999, priv. comm.), HCN (dashed contours) and 3 mm continuum emission (thick, dotted contours). The HCN emission is averaged from 8.81–11.8 km s<sup>-1</sup> and the contours are 3,5,7...  $\times 0.15$  Jy/beam ( $15.8'' \times 10.7''$  beam). The contours of the 3mm continuum image are 3,5,7...  $\times 2.5$  mJy/beam ( $15.5'' \times 10.5''$  beam).

Fig. 5.— Position–velocity plot along the C91 $\alpha$  filament (PA= 51°). The solid lines denote the positions of the three clumps labeled in Fig. 2. The C91 $\alpha$  emission is averaged over  $40''$  perpendicular to the filament and the contours are 3,5,7...  $\times 0.7$  mJy/beam ( $19.6'' \times 18.1''$  beam).

Fig. 6.— Channel images of the C91 $\alpha$  emission (thick contours, 3.2 mJy/beam spacings,  $19''$  beam) and the HCN emission (thin contours) on top of the HCO<sup>+</sup> emission shown in greyscale (both molecular lines with 1 Jy/beam spacings,  $15.8 \times 10.7''$  resolution, observed with BIMA). The filled square marks the position of the 3 mm continuum source.

Fig. 7.— Effelsberg 100m spectrum of the C65 $\alpha$  carbon recombination line observed at an offset position of (0'', -80'') from HD 37903.

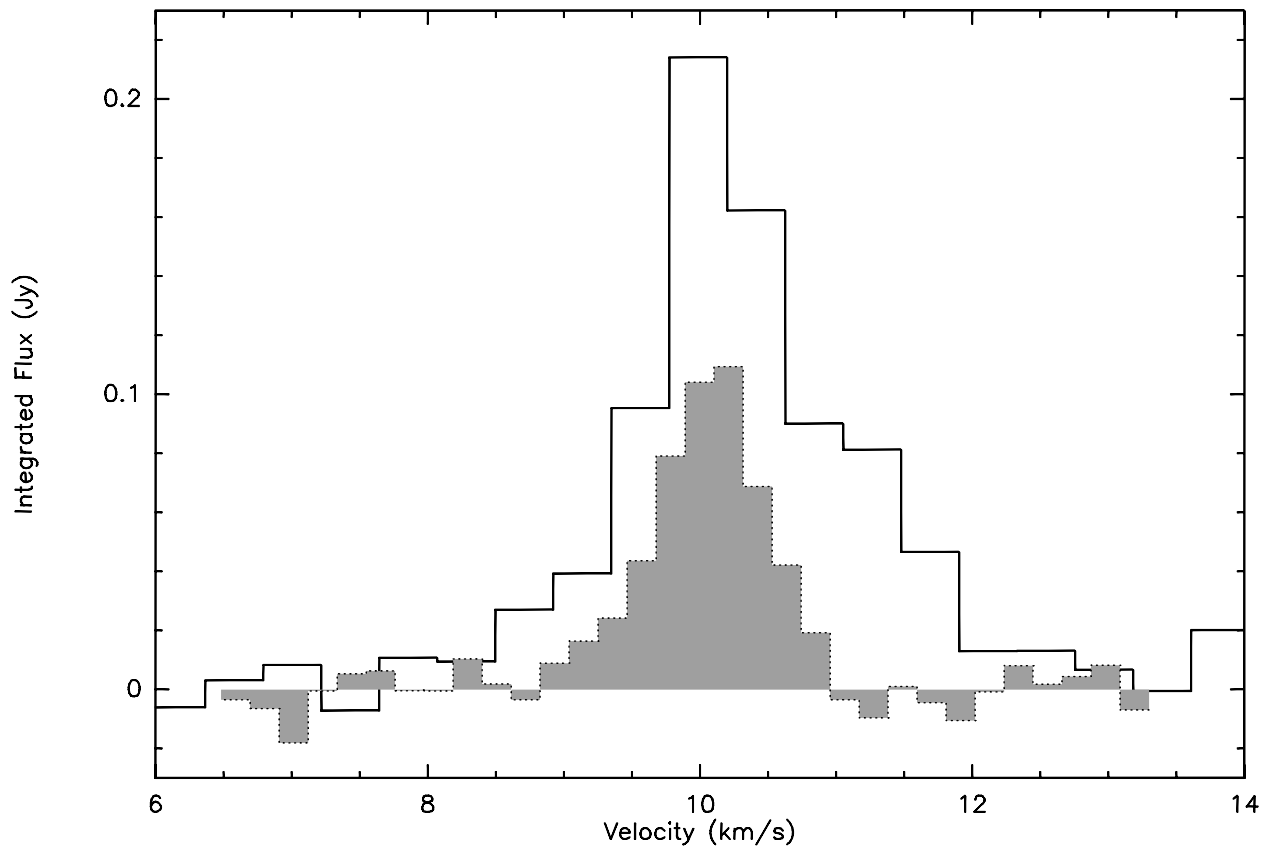
Fig. 8.— HCN and HCO<sup>+</sup> (grey-filled histogram) spectra averaged over  $20''$  regions centered on the offset positions ( $52'', -43''$ ) and ( $34'', -96''$ ). The HCN hyperfine satellite lines (at  $-7.1$  and  $4.9$  km s<sup>-1</sup>) are detected.

Fig. 9.— Ratio of HCN and HCO<sup>+</sup> emission (greyscale, steps of 0.1 from 0.3 to 0.8) overlaid on the integrated HCO<sup>+</sup> emission (contours: 30%,50%,70%... of the peak flux of 4.45 Jy/beam (15.8''×10.7'' beam)).

Fig. 10.— Cross-cuts through the C91 $\alpha$  clumps in C91 $\alpha$ , continuum, H<sub>2</sub><sup>\*</sup>, HCO<sup>+</sup> and HCN. In each panel the orientation of the cross-cut and the offsets of the clumps from HD 37903 are indicated.

Fig. 11.— Model results for an homogeneous edge-on PDR (Tielens & Hollenbach 1985) having  $n_{\text{H}} = 10^5 \text{ cm}^{-3}$ ,  $G_0 = 10^4$ , and  $X[\text{C}] = 1.4 \times 10^{-4}$ .

Fig. 12.— Carbon C91 $\alpha$  recombination lines towards several PDRs observed with the Effelsberg 100m telescope. The broad feature in the DR21 spectrum at 20 km s<sup>-1</sup> is the helium line from the prominent HII region.



### 8.5 GHz VLA observations of NGC2023

